SELF-ORGANIZED INTENSITY SPIRALS AND TARGET PATTERNS IN A SINGLE-MIRROR FEEDBACK SYSTEM

F. HUNEUS, T. ACKEMANN, W. LANGE

Institut für Angewandte Physik, Westfälische Wilhelms-Universität Münster
(Corrensstraße 2/4, D-48149 Münster, Germany;
e-mail: huneus@uni-muenster.de, t.ackemann@uni-muenster.de, w.lange@uni-muenster.de)

UDC 541.183

We report on experimental and theoretical investigations on spatio-temporal structures in a single-mirror feedback system using sodium vapor as the nonlinear medium. Target patterns and spirals with different numbers of arms are observed. A single spiral arm has an Archimedian shape. If the feedback mirror is tilted, the patterns transform to drifting segments of circles. It is shown that the appearance of these patterns depends on self-induced and externally applied spatial phase variations. For high order spirals, the oscillation amplitude vanishes at the beam center. Simulations indicate that the oscillating perturbations include a phase singularity at the beam center.

Rather complex and beautiful patterns can arise in optics due to the formation of caustics (e.g. [1 — 3]). The area of modern optics dealing with 'singularities in waves and rays' [1] is often termed 'singular optics' (e.g. [3]). Especially phase singularities displaying a local spiral phase structure around a point of zero intensity attracted a lot of attention [1, 3, 4].

In nonlinear optics, propagation and interference of waves are interrelated with nonlinearities. The combination of these two can lead to a variety of intriguing self-organization phenomena in the spatial distribution of intensity and phase. In particular, a lot of interest was triggered by the observation of Coullet et al. [5] that the Maxwell—Bloch equations describing the spatio-temporal dynamics of a laser admit solutions containing phase singularities of the optical field. These singularities were termed 'optical vortices' due to some analogies with hydrodynamics. Phase singularities were observed and analyzed in a variety of nonlinear optical systems including lasers, driven nonlinear cavities, and nonlinear beam propagation. Since it is impossible to give a proper account of the literature here, we refer to the corresponding reviews and special issues [6 — 11, 3]. These spiral patterns are *phase spirals* and thus are not directly observable with the eye or a camera. *Intensity spirals* are much less studied in optics. They were observed in nonlinear feedback systems in which the rotational symmetry is broken due to a rotation of the feedback loop [12 — 14], as well as in a system with rotational symmetry [15]. Intensity spirals were also predicted to occur in an internally pumped optical parametric oscillator [16].

However, the occurrence of phase as well as amplitude spirals is not confined to optical systems, but they are formed also in many non-optical pattern forming systems driven away from thermal equilibrium. Archetypal examples are chemical reactions [17, 18] and the chemotaxis of some biological specimens [19, 20]. Similar patterns occur also in electrochemistry [21], electro-luminescence of thin films [22], heterogeneous catalysis [23], Faraday experiments and convection instabilities [24]. In addition to spirals, systems of concentric rings – so-called target patterns – are observed in many systems. They can be thought of as spirals of order zero [25]. Phase spirals are important solutions of the complex Ginzburg-Landau equation [25]. Hence, the properties of optical spirals with their possibly universal or specific aspects are also very interesting from a general point of view.

In an earlier paper [15], we reported on the observation of target and spiral patterns in the intensity distribution transmitted by a single-mirror feedback scheme. The unstructured system has rotational symmetry. In contrast to the results obtained in other systems (see [26] for a recent exception) – the motion of the rings of a target pattern (or the arms of a spiral) is not directed outwards, but *inwards,* i.e. towards the core. It was shown that the drift direction is determined by nonlinear phase gradients, i.e. by phase gradients induced by the intensity profile of the pump beam. The drift direction can be reversed by introducing suitable phase distributions externally. Since, for the case of a plane wave input, the emergence of periodic structures like rhombs or hexagons is expected under the conditions of the experiment [27], these observations provide a striking example for a situation, in which the pattern forming process is totally changed by a spatial dependence of the control parameter which is the input intensity in this case.

In this paper, we will analyze the properties of the spiral patterns in more detail. We will also show how the spiral patterns react to a breaking of the parity symmetry, i.e. the introduction of a phase gradient by a tilt of the feedback mirror.

1. Experimental Setup

This work considers a special realization of the so-called single-mirror feedback scheme that was analyzed in [28 — 30]. Sodium vapor in a nitrogen buffer gas atmosphere is used as the nonlinear medium.

A schematic setup is shown in Fig. 1. The beam of a frequency-stabilized dye-jet ring laser provides the driving force needed for the formation of non-equilibrium conditions within the vapor. The light is typically 10 GHz 'blue'-detuned with respect to the sodium D_1-resonance. Its intensity can be adjusted by means of an electro-optical modulator. In order to obtain a smooth Gaussian-shaped intensity profile, the light field is spatially filtered using a single mode optical fiber. The beam radius at the $1/e^2$-point of intensity is approx. 1.5 mm corresponding to a Rayleigh length of about 12 m. The beam waist is located in the sodium vapor cell. Its polarization state is adjusted to be circular directly in front of the cell by means of a combination of a linear polarizer and a quarter-wave plate.

The cell is surrounded by three orthogonal pairs of Helmholtz coils to compensate for the Earth's magnetic field or to create an oblique dc magnetic field that changes the optical properties of the nonlinear medium. The sodium cell is held at a temperature T_{cell} of about 340° C and contains nitrogen buffer gas with a pressure of approximately 300—320 hPa.

The feedback mirror is located in the beam path at a distance d (typically 65 mm) behind the sodium vapor. It reflects more than 90 percent of the power back into the nonlinear medium and transmits only a small amount of light which is used for the analysis of the emerging structures.

The intensity distribution at a distance of $2d$ behind the mirror is imaged on one half of the chip of a charge-coupled device (CCD) camera. The field in this plane corresponds to the optical field reentering the nonlinear medium. We will refer to this as the near-field intensity distribution. The far-field distribution is supplied by a lens in a $2f$ scheme. A stop placed in the Fourier plane suppresses the central region around the wave number zero. After that, the Fourier plane is imaged on the other half of the CCD-camera. The camera is an analog video camera with an image intensifier. The digitized images

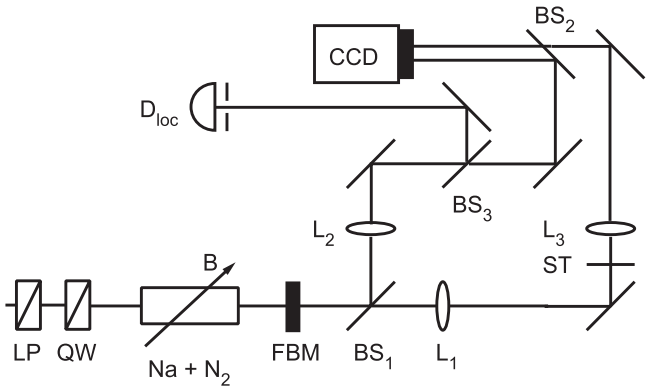

Fig. 1. Schematic experimental setup. LP — linear polarizer, QW — quarter-wave plate, FBM — feedback mirror, B — magnetic field, BS_1, BS_2, BS_3— beam splitters, L_1,L_2,L_3 — lenses, ST: stop

have a dynamic range of 8-bit and a spatial resolution of 768×576 pixels. A microchannel plate provides a fast shutter for the time-resolved acquisition of images of the near- and the far-field intensity distribution. In another arm of the setup, a small portion of the near-field image is sampled by a pinhole, which can be moved across the transverse cross section of the beam. The transmitted light is focused on a photodiode. Its amplified output signal is proportional to the local intensity. This signal can also be used as a trigger for the 'video-sampling method' that allows the recording of slow motion sequences of fast repetitive processes by scanning the delay between a trigger signal and the image acquisition [31, 32].

2. Experimental Characterization

When the laser power is increased, targets and spiral patterns are formed spontaneously beyond a certain threshold. Within the resolution of the current experiment, the bifurcation is continuous and without hysteresis, i.e. supercritical. Exemplary snapshots are presented in Fig. 2.

As is evident from the figure, various types of structures are observed, among them targets (Fig. 2,*a*), spirals with different chirality (Fig. 2,*b*,*c*), and spirals with different numbers of arms (Figs. 2,*c* to *h*). The structures are stable for periods of time between milliseconds and minutes. Spontaneous changes of the chirality or the number of spiral arms occur in a seemingly irregular manner. This may indicate a multi-stability of the different structures. The transitions between different structures are probably noise-driven.

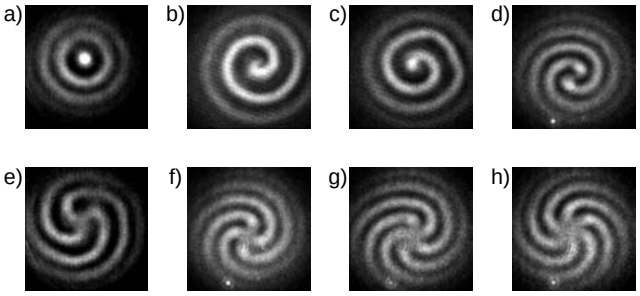

Fig. 2. Snapshots of structures spontaneously emerging in the transverse intensity profile of the laser beam for typical experimental parameters: *a* — target pattern, *b*, *c* — one-armed spirals with opposite chirality, *d*—*h* two- to six-armed spirals. The images are displayed in a linear grey-level coding with "black" denoting low intensity. The size of the images is between 2.6×2.6 and 3.0×3.0 mm^2

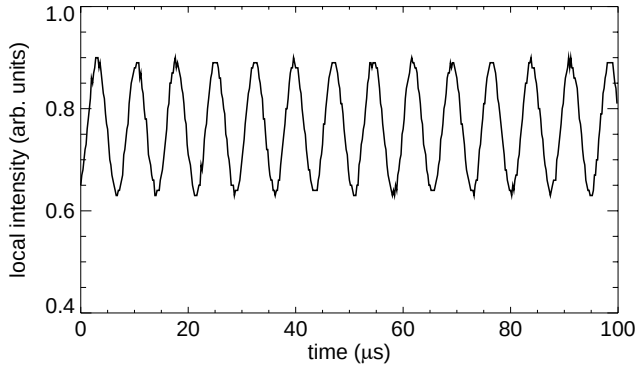

Fig. 3. Time trace of the local intensity obtained from the photo diode. Parameters: $d = 65$ mm, $\Delta = 9.8$ GHz, $B_\perp = 16.1\,\mu$T, $B_z = 43.2\,\mu$T, $T_{\rm cell} = 340°$C, $p_{N_2} = 312$ hPa, $P_{\rm in} = 108$ mW.

As already indicated above, the target patterns and spirals considered in this work are not stationary but dynamical structures. This is demonstrated by the output signal of the photodiode that indicates the temporal evolution of a local intensity. In Fig. 3, a time trace is presented that shows clearly the oscillatory and therefore dynamical character of this quantity.

The time series is periodic with a period of 7 μs. In fact, a power spectrum shows that it is even harmonic in a good approximation. Thus, one can assign a single frequency to the dynamics (here 143 kHz), which we will refer to as the 'characteristic' frequency in the following. Depending on parameters (especially the magnetic field), it ranges typically between some kHz and about 500 kHz. The quantitative form of the dependency of the characteristic frequency on the values of the transverse

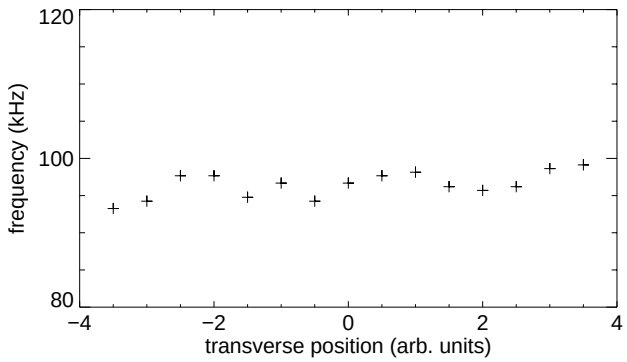

Fig. 4. Characteristic frequencies of the local intensity in dependency on the transverse position on the beam profile. Parameters: $d = 65$ mm, $\Delta = 18.6$ GHz, $B_\perp = 5.4\,\mu$T, $B_z = 30.9\,\mu$T, $T_{\rm cell} = 343°$C, $p_{N_2} = 309$ hPa, $P_{\rm in} = 173$ mW

and the longitudinal magnetic field component indicates that the oscillations can be interpreted as Larmor oscillations which are undamped by the feedback [33 — 35]). We comment on this in more detail in Sec. 3.

One can check for a spatial variation of the characteristic frequency across the beam diameter by laterally shifting the pinhole in front of the photo-diode across the cross section of the beam in the plane of the near-field image. Fig. 4 shows that the characteristic frequency fluctuates only within a few percent of a mean and no systematic variation can be detected. A possible origin of the variations are fluctuations of the magnetic field. Hence, the oscillation frequency of the local intensity seems to be constant across the diameter of the spirals and targets and we can use the characteristic frequency to characterize the time dependence of the total pattern. The distance between two spiral arms is typically of the order of 0.4 mm. Then, the measurement of the characteristic frequency gives a possibility to estimate the wave velocity, at least of the normal component. The velocity depends obviously on parameters, since the characteristic frequency is parameter dependent. It is of the order of some tens of meters per second (for the parameters of Fig. 3, it is about 57 m/s, for the parameters of Fig. 4 about 38 m/s).

Since the time dependence of the structures is periodic, it is possible to characterize the two-dimensional dynamics of the targets and spirals by means of the 'video-sampling method' [31, 32] using the signal of the local intensity as the trigger signal. In Fig. 5, snapshots from different phases of the motion are displayed. A sequence of images obtained in this manner

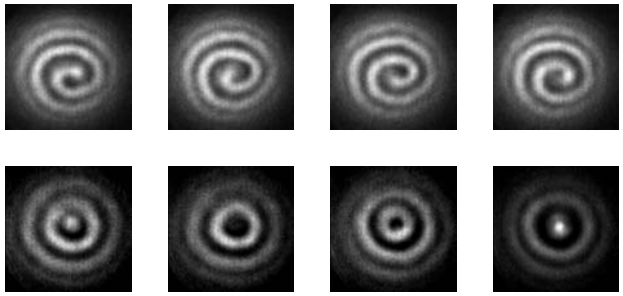

Fig. 5. Exemplary snapshots of an one-armed spiral (upper row) and a target pattern (lower row) taken from 'video sampling' sequences for typical parameters

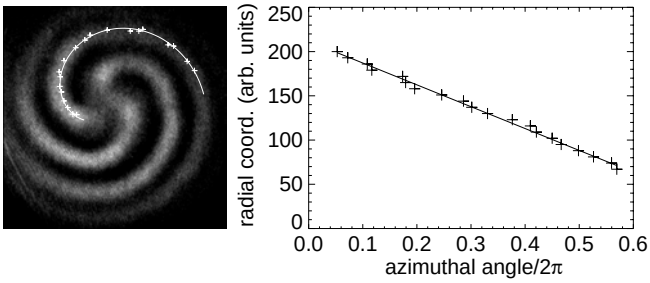

Fig. 6. Points belonging to the center line of a single spiral arm (left) and their radial coordinates in dependence on the azimuthal angle (right). The best-fitting linear relation is denoted as a solid line (both). Parameters: $d = 60$ mm, $B_\perp = 1.8\,\mu$T, $B_z = 7.5\,\mu$T, $T_{\rm cell} = 335°$C, $p_{N_2} = 205$ hPa, $P_{\rm in} = 93$ mW

reveals that the radial motion is directed inwardly. For a spiral, this results in an up-winding rotation of the structure while the concentric rings in a target pattern disappear at the center and new rings are created in the outer parts of the beam. This motion of the innermost ring can be seen nicely in the target pattern displayed in the lower row of Fig. 5. Another way to visualize the motion are space-time diagrams (see [15]). As mentioned in the introduction, this inward motion distinguishes the spirals and targets observed here from the spirals and targets observed in most of the other pattern forming systems that generate the corresponding pattern.

For a more precise characterization of the spirals, we take a closer look on the geometry of a single spiral arm. The recorded intensity distribution is converted to a binary image by thresholding at a suitable level. Then, a single arm is isolated. From azimuthal intensity profiles along rings with different radii, the points belonging to the center line of the arm are obtained. These are denoted by crosses in the left subpanel of Fig. 6. The graph on the right side of Fig. 6 shows the dependence of the radial coordinate on the azimuthal angle. The data points are described well by a linear relation. Hence, the spiral arm has the spatial shape of the trajectory of an object moving with constant radial and angular velocity, i.e. it has the shape of an Archimedian spiral. The best-fitting linear relation is plotted as a solid line in both subpanels of Fig. 6.

The intensity structures displayed in Fig. 2 result from contributions of the (nonhomogeneous) background field and the emerging structure. Due to the nonlinearities, these two contributions cannot be separated in a strict sense. However, we can try to separate the oscillating and stationary parts of the structures by averaging.

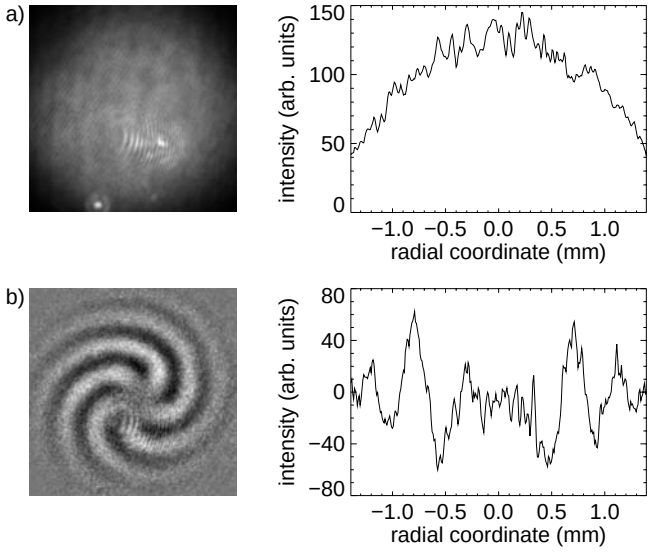

Fig. 7. *a* — time average of the images of a 'video sampling' sequence (left) and an intensity profile along a cut through the beam center (right). *b* — intensity distribution of the oscillating part of a five-armed spiral (left) and a profile along a cut through the beam center (right). Parameters: $d = 65$ mm, $\Delta = 12.9$ GHz, $B_\perp = 4.2\,\mu$T, $B_z = 14.4\,\mu$T, $T_{\rm cell} = 346°$C, $p_{N_2} = 314$ hPa, $P_{\rm in} = 135$ mW

The time average of the structure is obtained by adding images of a video-sampling sequence (as an example, we consider the spiral in Fig. 2,*g*). The averaged image is displayed in Fig. 7,*a*. The time average is rotationally symmetric and smooth except for some noise. The image in Fig. 7,*b* is obtained by subtracting the average from a snapshot, i.e. it represents the intensity distribution of the oscillating part of the structure. It has also the form of a spiral with the same number of arms as the original structure (here

five). Interestingly the center is zero (see the cut in the right part of Fig. 7,*b*), i.e. the oscillation vanishes at the center, which can be confirmed by direct inspection. The size of the central region decreases with the number of spiral arms as suggested by Fig. 2.

The peaks resulting from cuts through the spiral arms are approximately symmetric, i.e. there is no significant difference between the leading and the trailing edge of the wave.

After this characterization of the emerging dynamical structures based on experimental data, a theoretical analysis will be presented in the next section.

3. Theory

The experiment is modelled on the basis of a semiclassical description in which the light is interacting with a homogeneously broadened $J = \frac{1}{2} \leftrightarrow J' = \frac{1}{2}$ transition. This approach has been successfully applied many times before, so that only the main ideas are reviewed here. Details can be found in the literature [35 — 37].

Due to angular momentum selection rules, circularly polarized light creates a population difference between Zeeman substates of the ground state. This process is known as 'optical pumping' [39]. The resulting 'orientation' is proportional to the longitudinal component of the macroscopic magnetization of the sodium vapor. Here, "longitudinal" refers to the component of the magnetization parallel to the direction of light propagation, which we will refer to as the z-direction in the following and which we will regard as the quantization axis. The absorption coefficient and the refractive index depend linearly on this longitudinal component, which determines therefore the intensity dependent optical properties of the medium. In the presence of an external oblique magnetic field, the magnetization will precess and transverse components of the magnetization are generated, too. The state of the sodium vapor can be described by a Bloch-vector $\mathbf{m} = (u, v, w)$ that is proportional to the magnetic moment of the sample. The dynamical evolution of this quantity is governed by the partial differential equation [35 — 38]:

$$\frac{\partial}{\partial t}\mathbf{m} = -\gamma\mathbf{m} + D\Delta_\perp\mathbf{m} + \\ + \hat{\mathbf{e}}_z P(w, \Delta_\perp w) - P(w, \Delta_\perp w)\mathbf{m} - \mathbf{m}\times\Omega. \quad (1)$$

Here, γ is a constant relaxation rate of $\mathbf{m}$ of about 1.5 s^{-1}, D is the diffusion constant of the thermal diffusion of sodium atoms and $\Delta_\perp$ is the transverse part of the Laplacian. P is the pump rate for exciting sodium atoms. It provides a driving term for the z-component, only. The pump rate depends on w and $\Delta_\perp w$ due to the fact that the forward as well as the backward beam, i.e. the one reflected by the mirror, interact with the medium. The latter is modified in phase and amplitude due to the transmission through the medium and due to the diffraction taking place during propagation to the mirror and back. Free space propagation is described by the paraxial wave equation neglecting delay effects. P is assumed to be proportional to the sum of the intensities of the forward- and backward-travelling laser light. This is a reasonable approximation because effects due to the interference terms can be neglected due to the thermal motion of the sodium atoms. The origin of the next term is the saturation of optical pumping. Ω in the vector product is a torque vector defined by $\Omega = (\Omega_x, 0, \Omega_z - \bar{\Delta}P)$ where Ω_x and Ω_z are the Larmor frequencies connected to the respective components of the external magnetic field and the x-axis is chosen to be parallel to the transverse part of this quantity. Due to a light induced level shift, the z-component of Ω contains a term $-\bar{\Delta}P$ with $\bar{\Delta}$ being the suitably normalized detuning of the laser with respect to the D_1 resonance. The vector product describes the Larmor precession of the magnetization in the oblique magnetic field.

In [15, 27, 40], it was shown that the homogeneous solution of Eq. (1) becomes unstable against a Hopf bifurcation at a finite wave vector. This result is obtained from a linear stability analysis, in which the stability of the reference state is analyzed with respect to spatially periodic perturbations with a small amplitude. The length scale and frequency of these unstable modes match nicely the values obtained in the experiment indicating that this Hopf bifurcation is at the origin of the observed spatio-temporal instability. The existence of this bifurcation to an oscillating structure gives also some support to the procedure used in the previous section for a separation between the averaged structure – now interpreted to be connected to the reference state – and the oscillating structure – now interpreted as the bifurcating perturbation. However, we stress that a strict separation cannot be performed in the nonlinear stages of time evolution.

In the homogeneous system, the eigenmodes obtained in the linear stability analysis are transverse plane waves in strong disagreement with the experimental observations. Hence we study the dynamics in two spatial dimensions by numerical simulation including

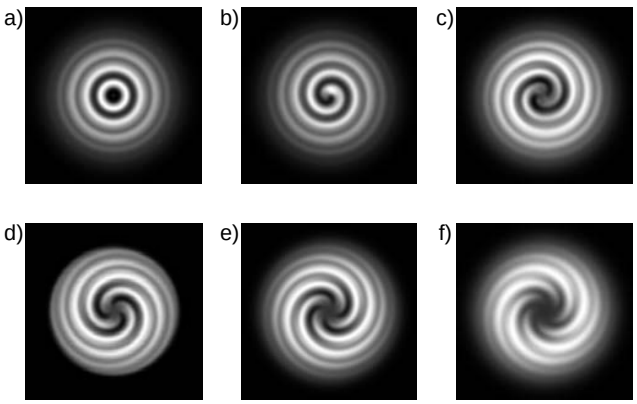

Fig. 8. Exemplary results of the two-dimensional numerical simulations. Presented are snapshots of the near-field intensity distribution. The displayed region has a size of $4.5 \times 4.5\,\mathrm{mm}^2$. Parameters: $P = 92500\ \mathrm{s}^{-1}$, $d = 70$ mm, $\Delta = 10.0$ GHz, $N = 0.8 \times 10^{20}\ \mathrm{m}^{-3}$, $D = 230\ \mathrm{mm}^2\,\mathrm{s}^{-1}$, $\gamma = 1.5\ \mathrm{s}^{-1}$, $\Gamma_2 = 10.1 \times 10^9\ \mathrm{rad\,s}^{-1}$; a — $\Omega_x = 2.0 \times 10^5\ \mathrm{rad\,s}^{-1}$, $\Omega_z = 10.0 \times 10^5\ \mathrm{rad\,s}^{-1}$, b — $\Omega_x = 4.0 \times 10^5\ \mathrm{rad\,s}^{-1}$, $\Omega_z = 12.0 \times 10^5\ \mathrm{rad\,s}^{-1}$, c, d — $\Omega_x = 2.0 \times 10^5\ \mathrm{rad\,s}^{-1}$, $\Omega_z = 8.0 \times 10^5\ \mathrm{rad\,s}^{-1}$, e — $\Omega_x = 2.0 \times 10^5\ \mathrm{rad\,s}^{-1}$, $\Omega_z = 7.8 \times 10^5\ \mathrm{rad\,s}^{-1}$, f — $\Omega_x = 2.0 \times 10^5\ \mathrm{rad\,s}^{-1}$, $\Omega_z = 7.5 \times 10^5\ \mathrm{rad\,s}^{-1}$

transverse boundary conditions and inhomogeneous pumping. A hopscotch algorithm is used for the temporal integration of the model equations. For describing the experiment as realistically as possible, the spatial shape of the pump rate distribution is taken to be Gaussian. The optical field reflected by the feedback mirror is calculated by a spectral method taking into account the finite reflectivity of the mirror: After Fourier transforming the light field transmitted by the medium, the propagation operator is applied in Fourier space and then the light field is inversely Fourier transformed. All fields in the simulations are discretized on a grid, typically 256×256 pixels sized representing an integration region of $6.0 \times 6.0\,\mathrm{mm}^2$. Temporally and spatially low-pass filtered noise is added to the pump rate. In order to model the destruction of orientation at the wall of the vapor cell, the Dirichlet boundary condition $\mathbf{m} = 0$ is used on a circular edge.

As shown earlier [15], the numerical simulations reproduce the emergence of the experimentally observed target patterns and spirals very well. Examples can be found in Fig. 8. The direction of motion is directed towards the center. Spirals with a higher number of arms are also obtained. It is apparent that the multiarmed spirals have an inner center with a low amplitude. The size of this area increases with the number of spiral arms. This matches the experimental observation (Fig. 2).

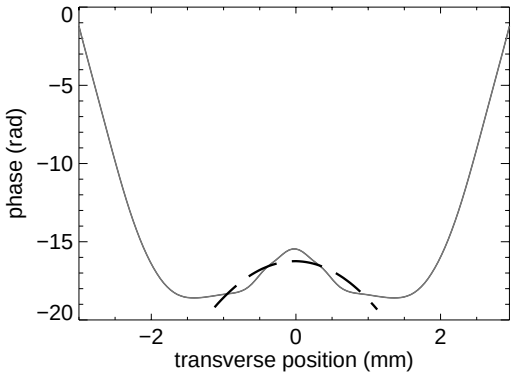

Fig. 9. Phase of the transmitted field in numerical simulations with a Fourier filter suppressing structuring. The dashed line is the parabola fitting best to the phase profile in the part of the beam exhibiting pattern formation without filter. Parameters: $d = 70$ mm, $\Delta = 9.0$ GHz, $\Omega_x = 1.0 \times 10^5\ \mathrm{rad\,s}^{-1}$, $\Omega_z = 12.0 \times 10^5\ \mathrm{rad\,s}^{-1}$, $N = 0.8 \times 10^{20}\ \mathrm{m}^{-3}$, $D = 312\ \mathrm{mm}^2\,\mathrm{s}^{-1}$, $\gamma = 1.0\ \mathrm{s}^{-1}$, $\Gamma_2 = 7.2 \times 10^9\ \mathrm{rad\,s}^{-1}$

In [15], it is shown that the radial profile of the input beam results in an inhomogeneous pumping of the medium. The induced refractive index profile creates a phase distribution of the transmitted beam, which resembles the one created by a defocusing lens within the region displaying pattern formation (Fig. 9). This is true "on average". This lens modifies the direction of motion of the waves and leads to the radial motion directed inwardly. We will discuss this in more detail in Sec. 4.

Spirals in nonlinear optical systems are usually connected to a spiraling phase distribution around a point of zero intensity. However, the center of the intensity spirals considered in the present work is always non-zero due to the background of the pump beam. It seems to be interesting to look in greater detail into the phase properties of these structures. In numerical simulations of the model equations, the optical field is easily accessible and thus it is analyzed in the following.

The phase distributions of the numerically simulated structures that are displayed in Fig. 8 are shown in Fig. 10. Neither for the target pattern (Fig. 10,*a*) nor for the spirals (Fig. 10,*b* to *h*), a phase singularity can be detected. For a target pattern, the phase is rotationally symmetric, while a small azimuthal variation but no steps of 2π are found in the case of a spiral. This is not surprising, since the intensity distribution is non-zero at the center.

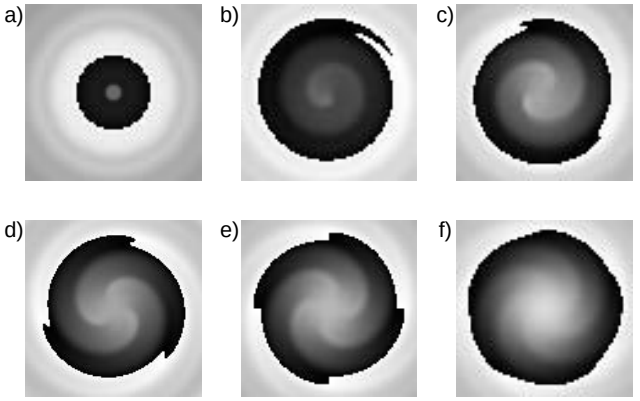

Fig. 10. Phase distributions of the numerically simulated structures displayed in Fig. 8. The central region is magnified. Parameters as in Fig. 8

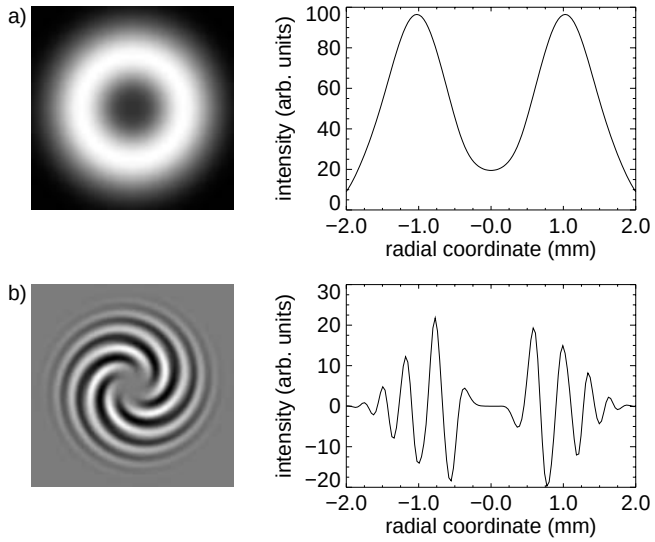

Fig. 11. Separation of the five-armed spiral (Fig. 8,*f*) in a stationary (*a*) and an oscillating part(*b*). On the left, the respective two-dimensional intensity distributions are shown, while on the right profiles along a cut through the center are displayed. Parameters as in Fig. 8,*f*

Again, as we did in Sec. 2., we separate the structure in a stationary and an oscillatory part by integration of a sequence of images and subtracting the normalized result from a single snapshot. For a five-armed spiral, the integrated picture is shown on the left side of Fig. 11,*a* and the subtracted image is presented on the left of Fig. 11,*b*.

On the right side of Fig. 11, intensity profiles along cuts through the center of the images are displayed. Although the integrated picture exhibits a nonlinearly induced minimum [37], the intensity distribution is not

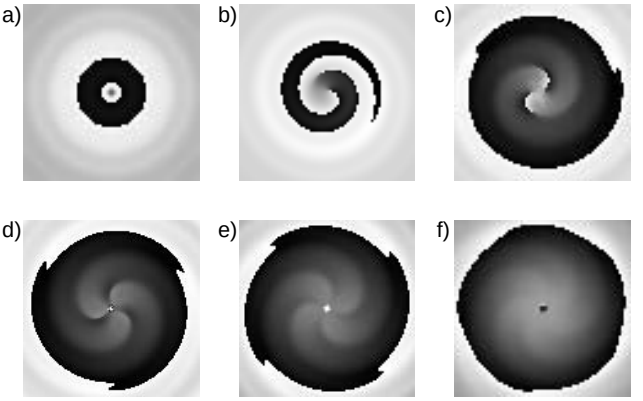

Fig. 12. Phase distributions of the electromagnetic field with the mean of the four central grid points subtracted as constant background for the structures displayed in Fig. 8. Magnification as in Fig. 10. Parameters as in Fig. 8

zero. In contrast, in the oscillating part, a region of zero intensity is now surrounded by a strong modulation. The separation of the structures into a constant and an oscillating part works fine for n-armed spirals with n greater than 3. However, since the unstructured and — with respect to the intensity — constant region in the center of the structure shrinks with decreasing number of spiral arms, no grid-point with non-oscillating time dependence can be found for a one- or two-armed spiral. We conjecture that this is due to an insufficient spatial resolution of the numerical grid in this case. We mention that the beam center (0,0) is not a grid point in our numerical scheme.

Although it cannot be proven for every structure, the extrapolation of the results obtained for spirals with many arms suggests that at least a single point at the center of the spiral with a low number of arms is kept at constant intensity during the oscillation. Therefore one could think of subtracting a constant background when considering the optical field. The resulting phase distributions obtained after this procedure are depicted in Fig. 12.

As expected, the phase of the target pattern has still no azimuthal modulation (Fig. 12,*a*). But now, when moving on a circle around the center of Figs. 12,*b* and c, one or two steps of 2π are encountered, respectively. For the three- (Fig. 12,*d*), four- (Fig. 12,*e*) and five-armed spirals (Fig. 12,*f*), some phase variations at the center in the three- and four-fold symmetric cases can be detected, but there is no clear signature of phase singularities. We conjecture that the numerical grid is too coarse to map the abrupt variations of the phase. There is obvious

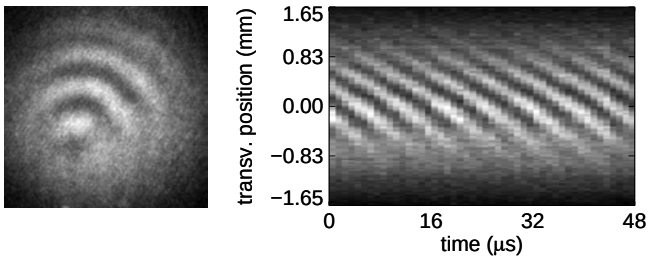

Fig. 13. Ring segments moving to the central part of the beam for a tilted feedback mirror. A near-field image (left) and a space-time-diagram illustrating the radial motion (right) are presented. Parameters: $d = 65$ mm, $\Delta = 5.8$ GHz, $B_\perp = 7.7\,\mu$T, $B_z = 28.8\,\mu$T, $T_{\rm cell} = 342°$C, $p_{N_2} = 320$ hPa, $P_{\rm in} = 91$ mW

need for a clarification by more elaborate numerical simulations.

Thus, although the phase distribution of the whole structure is smooth, phase singularities, which seem to have a charge equal to the number of spiral arms, become visible at the center of the oscillating part of the spirals, if the optical field there is subtracted as a constant background. This needs to be investigated in more detail in a future work.

4. Tilt of Feedback Mirror

As we have already mentioned in Sec. 3., phase gradients have a fundamental influence on the target patterns and spirals observed in this system. The selection of the oscillating structures is due to nonlinearly induced phase gradients generated by the Gaussian intensity profile of the laser beam (see Fig. 9 and [15]). In [15], it was also reported that the compensation of this self-induced lens by an externally applied suitable phase distribution enables the formation of stationary hexagons, while an overcompensation reverses the direction of the radial motion. Then, instead of inwardly moving structures, outwardly moving ones can be observed.

Because of the crucial role of spatial phase variations in the present system, we will discuss the consequences of an interaction of the self-induced phase distribution with an externally applied linear phase gradient in the following. Experimentally, this is realized by a tilt of the feedback mirror. In that case, forward and backward beams are no longer exactly counterpropagating and there is a displacement of the reflected light field. It is known that such a tilt, respectively shift, causes a drift motion of periodic patterns or localized states, which are stationary otherwise [41, 42, 13, 43 — 46].

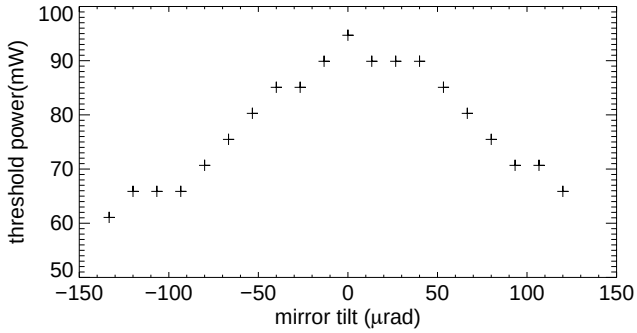

Fig. 14. Experimentally determined threshold for pattern formation in dependence on the tilt angle of the feedback mirror. Parameters: $d = 65$ mm, $\Delta = 11.0$ GHz, $B_\perp = 10.1\,\mu$T, $B_z = 29.5\,\mu$T, $T_{\rm cell} = 345°$C, $p_{N_2} = 313$ hPa

In the experiment, no target patterns or spirals are formed at the threshold, when the feedback mirror is tilted and the laser power is increased, but typically structures similar to the ones shown in the left subpanel of Fig. 13 are observed. Segments of concentric rings fill a sector on that side of the transverse cross-section of the laser beam to which the reflected light is shifted. The length scale is that of the target patterns and spirals. If the local intensity at one point within this sector is monitored through the pinhole, a periodic signal is observed. This demonstrates that these ring fragments are dynamical structures, too.

Intensity profiles along cuts through images of a 'video-sampling' sequence are arranged in the right part of Fig. 13 to form a space-time diagram that describes the motion of the waves. The drift is directed antiparallel to the displacement of the backward traveling laser light. That means that the rings are born in the outer parts of the light field and move towards the central part where they disappear. During this motion, the angular extension of each ring shrinks to a small area, possibly a single spot, just before it vanishes.

Interestingly, these moving ring segments are formed at lower values of the laser power than the spirals and targets do. The plot displayed in Fig. 14 reports a systematic investigation of this phenomenon.

The experimentally determined threshold power for pattern formation is shown in dependence on the tilt of the feedback mirror. A single maximum of the threshold power is observed. Starting from this mirror position, the threshold decreases monotonically if the tilt is changed. Since we cannot identify the optimal alignment condition by independent means and because of the

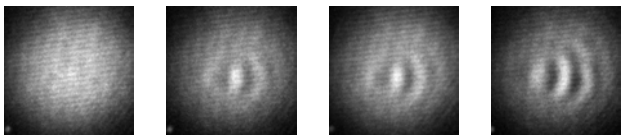

Fig. 15. Experimental snapshots of dynamical ring segments for increasing tilt angles of the feedback mirror. The tilt angles are from left to right: 53 μrad, 67 μrad, 80 μrad and 93 μrad. $P_{\rm in}$ = 80 mW, other parameters as in Fig. 14

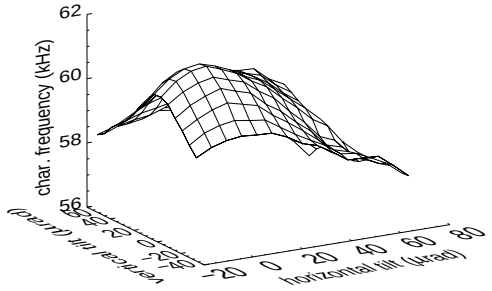

Fig. 16. Distribution of the characteristic frequencies in dependency on the horizontal and vertical tilt of the feedback mirror in the experiment. Parameters: $d = 65$ mm, $\Delta = 10.6$ GHz, $B_\perp = 4.2\,\mu$T, $B_z = 13.0\,\mu$T, $T_{\rm cell} = 339°$C, $p_{N_2} = 315$ hPa, $P_{\rm in} = 120$ mW

approximate symmetry of the plot, we assume that the maximal threshold power for pattern formation corresponds to the rotationally symmetric system, i.e. to the optimal alignment conditions. The structures developing in that case are spirals or targets.

In Fig. 15, a sequence of snapshots obtained at different tilt angles is displayed. The power level is kept below the threshold for pattern formation in the optimal alignment condition (leftmost image in Fig. 15), hence there is no structure.

If the mirror is tilted above some threshold value, a weakly modulated structure moving to the left can be found in a small portion of the transverse cross-section (second image in Fig. 15). This sector widens and the modulation of the structure becomes more pronounced in the next images displaying the structures for a larger tilt angle. In the last image, the pattern can be interpreted as consisting of segments of concentric rings.

We analyzed also the dependence of the characteristic frequency on the tilt angle by Fourier transforming time traces of the local intensity. The smoothed result of a two-dimensional scan of the tilt angle is presented in Fig. 16 (the power level was

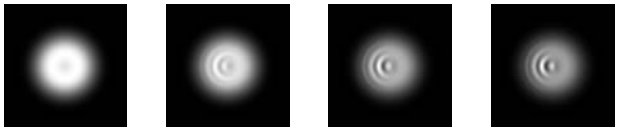

Fig. 17. Images of dynamical ring segments for increasing displacement of the reflected optical field in numerical simulations. Displacements are from left to right: 0 μm, 2 μm, 4 μm, 6 μm. The numerical grid size is 128 × 128 pixels; other parameters: $P = 75000\ {\rm s}^{-1}$, $d = 70$ mm, $\Delta = 10.0$ GHz, $\Omega_x = 4.0\times10^5\ {\rm rad\,s}^{-1}$, $\Omega_z = 1.2\times10^5\ {\rm rad\,s}^{-1}$, $N = 0.8\times10^{20}\ {\rm m}^{-3}$, $D = 230\ {\rm mm}^2\,{\rm s}^{-1}$, $\gamma = 1.5\ {\rm s}^{-1}$, $\Gamma_2 = 10.1\times10^9\ {\rm rad\,s}^{-1}$

adjusted such that there is the pattern formation for optimal alignment). The distribution of the characteristic frequencies exhibits a small but seemingly systematic variation. It is single-humped and decreases monotonically in all directions.

In the following, we will compare these experimental observations with two-dimensional numerical simulations of the model equations.

In Fig. 17, images of the emerging structures for different displacements of the reflected field are displayed. There is no pattern formation for optimum alignment (leftmost image in Fig. 17). If a sufficiently large displacement is present, we observe the development of segments of concentric rings appearing on the side of the beam to which the shift is directed (second image in Fig. 17). The waves move antiparallel to the shift of the backward beam. If the displacement is increased, the modulation amplitude of the structures grows and the sector in which they appear widens (images on the right of Fig. 17). This sequence of images corresponds nicely to the one obtained experimentally (Fig. 15).

The numerical simulations confirm that indeed the rotational symmetric system has the highest threshold for pattern formation. With increasing displacement, the threshold decreases as seen in Fig. 18 where the threshold power is depicted in dependence on the displacement. Just as in the experiment (Fig. 14), the threshold decreases monotonically with increasing tilt. While the threshold pump rate is about $78000\ {\rm s}^{-1}$ in the aligned system, only a pump rate of about $52500\ {\rm s}^{-1}$ is needed to form structures in the presence of a 20 μm displacement which corresponds to a mirror tilt of 143 μrad. This amounts to a reduction to 67%. In the experiment, a reduction to 65% is obtained for a tilt of about 135 μrad, i.e. there is also a nice correspondence concerning the magnitude of the effect.

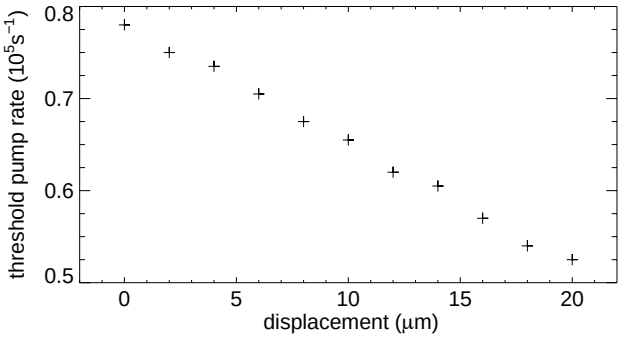

Fig. 18. Threshold of the formation of dynamical structures in dependence on the displacement of the reflected light field. Parameters as in Fig. 17

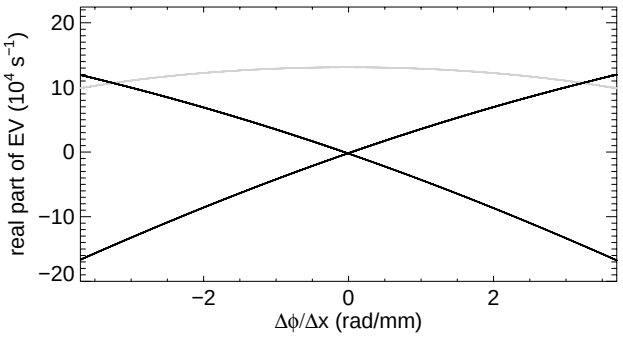

Fig. 19. Real parts of the eigenvalues calculated in the linear stability analysis for a stationary (grey) and two Hopf modes (black) in dependence on the strength of a phase gradient. Parameters: $P = 92500$ s^{-1}, $d = 70$ mm, $\Delta = 9.0$ GHz, $\Omega_x = 1.0 \times 10^5$ rad s^{-1}, $\Omega_z = 1.2 \times 10^5$ rad s^{-1}, $N = 0.8 \times 10^{20}$ m^{-3}, $D = 312$ mm^2 s^{-1}, $\gamma = 1.0$ s^{-1}, $\Gamma_2 = 7.2 \times 10^9$ rad s^{-1}

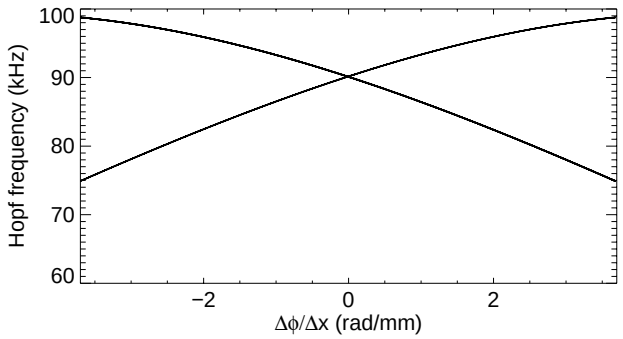

Fig. 20. Frequencies calculated from the absolute values of the imaginary parts of the eigenvalues for the two Hopf modes. The increasing frequency corresponds to the mode with the decreasing real part of the eigenvalue in Fig. 19 and vice versa. Parameters as in Fig. 19

For a better understanding of the experimental and numerical observations reported above, a linear stability analysis of the homogeneous solution is performed that takes into account a shift of the reflected light field. In Fig. 19, the growth exponents (i.e. the real part of the eigenvalues) for the three modes with the highest growth rates are shown in dependence on the displacement of the backward beam. For zero displacement, the mode with the highest growth rate has zero imaginary part. The two other modes have nonzero imaginary parts and the eigenvalues are the complex conjugate of each other. We will refer to them as 'stationary' and 'Hopf' modes in the following. If a displacement is introduced, the growth rate of the stationary mode is reduced (it acquires also a small imaginary part which reflects the induced drift mentioned above). In addition, the symmetry between the two Hopf modes is broken. The growth rate of one of them is increased, whereas the other one is decreased. For a sufficiently large displacement (here about 3.2 rad/mm), the growth rate of the favored Hopf mode is larger than the growth rate of the stationary mode.

Since the eigenvalues are complex conjugated in the rotational symmetric case, the frequencies of the two Hopf modes have the same absolute value even though the imaginary parts, of course, have opposite signs. This changes in the presence of a phase gradient, as it can be seen in Fig. 20. It turns out that the frequency of the mode with the increasing growth exponent decreases and vice versa.

For the favored mode, the phase velocity $\mathbf{v} = \mathrm{Im}(\eta) \cdot \mathbf{q}_\perp / |\mathbf{q}_\perp|^2$ is directed antiparallel to the displacement, while it is directed parallel for the disfavored mode. Here, η is the eigenvalue of the mode and $q_\perp$ the transverse wave vector.

From these results, it is possible to conclude that oscillating structures are more likely to emerge if there is a large phase variation. In [15], an argument of this kind was used to explain the preference of the oscillating structure versus the stationary ones for the case of rotational symmetry. The relevant variation in that case is the variation in the background phase due to the Gaussian shaped pump profile (see Fig. 9). On each side of the beam center, one might approximate the phase profile even by a linear gradient, although this is of course a rather crude approximation. Then, the considerations done above apply and the linear stability analysis predicts waves propagating in the direction

of the gradient, i.e. inwardly. This is indeed what is observed in the experiment.

In the situation considered here, the rotationally symmetric phase variations self-induced by the Gaussian pump beam and the linear gradient due to the mirror tilt add up. There will be one direction, in which they add up constructively, whereas, in the opposite direction, the two phase distributions tend to compensate each other. It is possible to conclude from Fig. 19 that the threshold for pattern formation in the former case is lower (the growth rate is higher) than in the latter case. Hence it is expected that the pattern formation will start at one side of the beam and indeed this is what is observed in the experiment and in the simulations. It is also obvious that the threshold in the presence of a tilt will be lower than without a tilt. When the tilt of the feedback mirror is increased, the linear phase gradient is enforced and the growth coefficient of the favored Hopf mode becomes larger. This leads to a broadening of the sector where the Hopf mode is undamped. This feature is also obtained in the experiment as well as in the simulations.

Finally, the experimentally observed distribution of the characteristic frequencies (Fig. 16) can also be understood. Since the frequency of the favored Hopf mode is reduced (Fig. 20), if the tilt of the mirror is increased, the characteristic frequency decreases.

Summary and Conclusions

In this paper, we have reported on the properties of spiral and target patterns in a simple pattern forming optical system. The properties of the waves depend crucially on the background phase distribution. This can be nicely illustrated by the study of the interplay between the rotationally symmetric variations (nonlinearly induced by the pump profile) and a linear gradient (imposed externally by a tilt of the feedback mirror). Since self-induced as well as externally imposed inhomogeneities exist in many nonlinear optical systems, we expect that this mechanism might be relevant also in other systems. For example, some of the observations reported in [13, 14] bear some similarities to the case discussed here.

Since the observed structures are formed from a combination of the background field and the bifurcating structure, the total intensity does not vanish. Hence, the structures do not contain phase singularities. However, our analysis suggests that the bifurcating oscillating structure might be described in terms of modes with a $\exp(im\phi)$ dependence. This will be the subject of further investigations.

1. *Berry M.V.*/Physics of Defects./Ed. by R. Balian.— Amsterdam: North-Holland, 1981.— (Vol. XXXV of Les Houches Session).
2. *Berry M.*// Nature.—2000.—**403**.— P.21.
3. *Soskin M.S., Vasnetsov M.V.*// Progr. in Optics.—2001.— **42**.— P.219—276.
4. *Optical* vortices /Ed. by M. Vasnetsov, K. Staliunas.— Commack, NY: Nova Science Publ., 1999.— (Vol. 228 of Horizons in World Physics).
5. *Coullet P., Gil L., Rocca F.*// Opt. Communs.— 1989.— **73**.— P.403—408.
6. *Lugiato L.A.*// Phys. Repts.— 1992.— **219**.— P.291—310.
7. *Weiss C.O.*// Ibid.— P.311—338.
8. *Lugiato L.A.*// Chaos, Solitons & Fractals.— 1994.— **4**.— P.1251—1258.
9. *Lugiato L.A., Brambilla M., Gatti A.*// Adv. Atom. Mol. Opt. Phys.— 1999.— **40**— P.229—306.
10. *Arecchi F.T., Boccaletti S., Ramazza P. L.*// Phys. Repts.— 1999.— **318**.— P.1—83.
11. *Weiss C.O., Vaupel M., Staliunas K. et al.*// Appl. Phys. B.— 1999.— **68**.— P.151—168.
12. *Akhmanov S.A., Vorontsov M.A., Ivanov V.Yu.*// Sov. Phys. JETP Lett.— 1988.— **47**— P.707—711.
13. *Akhmanov S.A., Vorontsov M.A., Ivanov V.Yu. et al.*// J. Opt. Soc. Amer. B.— 1992.— **9**.— P.78—90.
14. *Rehn H., Kowarschik R.*// Opt. Lett.— 1996.— **21(18)**.— P.1505—1507.
15. *Huneus F., Schäpers B., Ackemann T., Lange W.*// Appl. Phys. B.—2003.—**76**.—P.191—197.
16. *Lodahl P., Bache M., Saffman M.*// Phys. Rev. Lett.—2000.— **85**.— P.4506—4509.
17. *Winfree A.T.*// Science.—1972.—**175**.— P.634–636.
18. *Ross J., Müller S.C., Vidal C.*// Ibid.—1988.— **240**.— P.460—465.
19. *Gerisch G.*// Naturwissenschaften.— 1971.— **58**.— P.430—438.
20. *Steinbock O., Hajime Hashimoto, Müller S. C.*// Physica D.— 1991.—**49**.—P.233—239.
21. *Agladze K., Steinbock O.*// J. Phys. Chem.—2000.— **104**.— P.9816—9819.
22. *Goßen Ch., Niedernostheide F.J., Purwins H.G.* Pattern Formation of the Electroluminescence in AC ZnS:Mn Devices.— Berlin, Heidelberg: Springer, 1995.
23. *Jakubith S., Rotermund H.H., Engel W. et al.*// Phys. Rev. Lett.—1990.— **65**.— P.3013—3016.
24. *Assenheimer M., Steinberg V.*// Nature.— 1994.— **367**.— P.345—347.
25. *Aranson I.S., Kramer L.*// Rev. Mod. Phys.— 2002.— **74**.— P.99—143.
26. *Vanag V.K., Epstein I.R.*// Science.— 2001.— **294**.— P.835—837.
27. *Logvin Yu.A., Ackemann T.*// Phys. Rev. E.— 1998.— **58**.— P.1654—1661.

28. *Firth W.J.*// J. Mod. Opt.— 1990.— **37**.— P.151—153.

29. *D'Alessandro G., Firth W.J.*// Phys. Rev. Lett.— 1991.— **66**.— P.2597—2600.

30. *D'Alessandro G., Firth W.J.*// Phys. Rev. A.— 1992.— **46**.— P.537—548.

31. *Möller W. J., Bruns H.J.*// Rev. Sci. Instrum.— 1995.— **66**.— P.4535—4538.

32. *Möller M., Seipenbusch J.P., Ackemann T. et al.*// Chaos, Solitons & Fractals.— 1999.— **10**.— P.675—679.

33. *Kitano M., Yabuzaki T., Ogawa T.*// Phys. Rev. A.— 1981.— **24**.— P.3156—3159.

34. *Mitschke F., Mlynek J., Lange W.*// Phys. Rev. Lett.— 1983.— **50**.— P.1160—1663.

35. *Mitschke F., Deserno R., Lange W., Mlynek J.*// Phys. Rev. A.— 1986.— **33**.—P.3219—3231.

36. *Ackemann T., Logvin Y., Heuer A., Lange W.*// Phys. Rev. Lett.— 1995.— **75**.— P.3450—3453.

37. *Ackemann T., Heuer A., Logvin Yu. A., Lange W.*// Phys. Rev. A.— 1997.— **56**.— P.2321—2326.

38. *Lange W., Ackemann T.*// Asian J. Phys.— 1998.— **7**.— P.439—452.

39. *Kastler A.*// J. Opt. Soc. Amer.— 1957.— **47**.— P.460—465.

40. *Logvin Yu.A., Ackemann T., Lange W.*// Europhys. Lett.— 1997.— **38**.— P.583—588.

41. *Haelterman M., Vitrant G.*// J. Opt. Soc. Amer. B.— 1992.— **9**.— P.1563—1570.

42. *Rosanov N.N.*// Proc. SPIE.— 1991.— **1840**.— P.130—143.

43. *Grynberg G.*// Opt. Communs.— 1994.— **109**.— P.483—486.

44. *Ramazza P.L., Bigazzi P., Pampaloni E. et al.*//Phys. Rev. E.— 1995.— **52**.— P.5524—5531.

45. *Firth W.J., Scroggie A.J.*//Phys. Rev. Lett.— 1996.— **76**.— P.1623—1626.

46. *Seipenbusch J.P., Ackemann T., Schäpers B. et al.*// Phys. Rev. A.— 1997.— **56**.— P.R4401—R4404.

СПОНТАННЕ ВИНИКНЕННЯ СПІРАЛЕЙ ІНТЕНСИВНОСТІ ТА РЕГУЛЯРНИХ СТРУКТУР В СИСТЕМАХ ЗВОРОТНОГО ЗВ'ЯЗКУ З ОДНИМ ДЗЕРКАЛОМ

Ф. Хюнеус, Т. Акеманн, В. Ланге

Р е з ю м е

Описано експериментальні та теоретичні дослідження просторово-часових структур в однодзеркальній системі зворотного зв'язку із використанням парів натрію у ролі нелінійного середовища. Спостерігались регулярні структури та спіралі з різною кількістю рукавів. Спіраль з одним рукавом має архімедову форму. Якщо змінювати нахил дзеркала зворотного зв'язку, то картина буде змінюватись шляхом зміщень сегментів кола. Показано, що виникнення таких картин залежить від самоіндукованих та нав'язаних ззовні просторових змін фази. Для спіралей високого порядку амплітуда осциляцій в середині пучка дорівнює нулеві. Розрахунки показують, що збурення осциляції в центрі пучка має фазову сингулярність.